Hot-Carrier Effect and Nanometer Metal Enabling Si-Based Mid-Infrared Detection Beyond 5μm of Wavelength

Zih-Chun Su, *Member, IEEE*, Yao-Han Dong, *Member, IEEE*, and Ching-Fuh Lin, *Fellow, IEEE*

***Abstract*—Detection of photons with energy below the bandgap or Schottky barrier height of silicon has been limited in the past. Here, we reveal an approach that harnesses hot carriers through diffusion over a very thin metal to achieve silicon-based mid-infrared detection. With strong localized surface plasmon resonance (LSPR) effect to enhance infrared absorption and diffusion across 10 nm metal in Schottky structure, the hot carriers can be effectively collected. Such mechanism leads to responsivity from 0.098 mA/W to 0.237 mA/W for the wavelengths between 2700 nm and 5300 nm, all corresponding to photon energy below Schottky barrier height. Our investigation further shows that inverted pyramidal structures could enhance LSPR and so the responsivity. In addition, this approach enables us to monitor high frequency optical signals up to 2.1 MHz. By harnessing hot carriers and enhancing LSPR, we have not only overcome previous limitations in silicon-based mid-infrared detection but also opened up new possibilities for advanced photonics and optoelectronics applications.**

***Index Terms*—Localized surface plasmon resonance, mid-infrared (MIR) detectors, MIR sensors, photodetectors, silicon, silicon photonics, Schottky devices, Schottky diodes, Ultra-broadband infrared photon detection technique.**

I. Introduction

INFRARED detection is important for diverse applications due to its ability to sense and detect wavelengths beyond the human eye's range ($\lambda > 800$ nm). Fields such as atomic physics [1], astronomy [2], and medicine [3], [4], [5] rely heavily on broadband optical detection, particularly in the mid-infrared range. The past works have focused on mid-infrared photonic integrated circuit sensing platforms based on material such as narrow-gap semiconductors (InGaAs [6], [7], [8], [9], InAs [10], InSb [11], Ge [12], and HgTe [13]), tunable energy-gap 2D materials [14], [15], and heterostructures of narrow-gap semiconductors (quantum well structures and superlattices [16], [17]). However, integrating these materials with silicon is challenging due to the lattice mismatch, which requires finely controlled epitaxial fabrication and longer process durations [18]. To address this, Si-based infrared detection ideas have been proposed, such as antenna-assisted Silicon waveguide-based bolometers [19], [20], which rely on the reflective spectra [21] or thermal conductivity to achieve mid-infrared sensing on silicon, but their response speed is typically slower than 3 μs [19], [20].

As a low-cost and high-sensitive alternative, the Schottky devices with LSPR effect which have the advantage of easy integration with complementary metal-oxide semiconductor transistors [22], [23] are excellent candidates for Si-based mid-infrared detection. Although metals have the potential to develop infrared sensing because of their non-energy gap properties that allow full-band photon absorption, thick metals may reflect the light strongly and exhibit long transportation time. Therefore, the thickness of the metal absorbing layer needs to be controlled at the nanometer scale. In recent years, there have been many discussions between the hot carrier effect with LSPR and nanoscale metal material on the near-infrared band spectrum response [24], [25]. In 2017, Zhiyang et al. [24] proposed an Au nanoparticle covered silicon structure with photoresponsivity at the wavelength range of 1200−1475 nm. The relation between responsivity and location of excited hot carrier has also been demonstrated by Yusheng et al. [25]. To detect spectrum response longer than 1700 nm, the photodetector responsivity is improved by the LSPR-induced structure, which traps incident photons and covers from 300 to 2700 nm [26]. However, these studies focus on the design of structures in the visible and near-infrared spectral bands, combining internal light emission mechanisms to investigate infrared light detection. There are still technical bottlenecks in the research of the infrared spectral band for lower energy photons. To detect photons with energy lower than the Schottky barrier height, further exploration of the dynamics of the hot carrier interactions is necessary.

Here we report on the discovery of mid-infrared light detection using a Schottky diode that incorporates a hot-carrier effect, a nanoscale metal material and a LSPR structure. The planar Cr/n-Si Schottky device could only detect mid-infrared light with responsivities in the range of nA/W to μA/W. However,

Manuscript received 4 April 2024; revised 22 April 2024; accepted 26 April 2024. Date of publication 1 May 2024; date of current version 13 May 2024. This work was supported in part by the Ministry of Science and Technology (MOST) and in part by the National Science and Technology Council (NSTC) in Taiwan under Grant MOST 108-2221-E-002-145-MY3/MOST 110-2218-E-002-032 -MBK/MOST 111-2218-E-002-019 -MBK/MOST 111-2221-E-002 -080 -MY3/NSTC 112-2218-E-002-035-MBK. *(Zih-Chun Su and Yao-Han Dong contributed equally to this work.) (Corresponding author: Ching-Fuh Lin.)*

Zih-Chun Su and Yao-Han Dong are with the Graduate Institute of Photonics and Optoelectronics, National Taiwan University, Taipei 106319, Taiwan (e-mail: f06941006@ntu.edu.tw; f09941116@ntu.edu.tw).

Ching-Fuh Lin is with the Graduate Institute of Photonics and Optoelectronics, National Taiwan University, Taipei 106319, Taiwan, and with the Graduate Institute of Electronics Engineering, National Taiwan University, Taipei 106319, Taiwan, and with the Department of Electrical Engineering, National Taiwan University, Taipei 106319, Taiwan, and also with the Center for Electronics Technology Integration, National Taiwan University, Taipei 106319, Taiwan (e-mail: lincf@ntu.edu.tw).

Digital Object Identifier 10.1109/JPHOT.2024.3395982

© 2024 The Authors. This work is licensed under a Creative Commons Attribution 4.0 License. For more information, see https://creativecommons.org/licenses/by/4.0/

introducing a strong LSPR structure increases the responsivities to near mA/W scale. This mechanism also enabled detection of wavelengths up to 5.3 μm with a response of up to 0.237 mA/W, which broadens the detection spectrum, compared to the planar device. Notably, this mechanism is different from the photo-thermoelectric (PTE) mechanism that detects infrared signals based on photothermal conversion and thermoelectric effect. It allows us to achieve 2.1MHz frequency response without sacrificing responsivity. Based on these advantages, Schottky junction with hot-carrier effect provides an opportunity to realize low-cost, silicon-based broadband infrared light detection.

II. Materials and Methods

In previous research, we focused on planar metal-insulator-semiconductor structures [27], [28], successfully reducing the Fermi level pinning effect and lowering the Schottky barrier, thus enhancing the responsivity of device. Based on the results from planar devices, hot carrier Schottky devices are capable of detecting tiny mid-infrared optical signals. In this work, we further increased the incident light absorption of the device and explored methods to collect hot carriers before decay, aiming to achieve the detection of low-energy photons. To increase the incident light intensity on the silicon substrate with wavelengths ranging from nanometers to micrometers, a periodic array of inverted pyramid structures (IPS) was fabricated on the surface of hot carrier device. At the same time, the thickness of the Schottky metal was controlled at 10 nm to prevent reflection from metal, ensuring that hot carriers are able to cross the Schottky interface before decay. To improve the signal-to-noise ratio (SNR) and reduce the Schottky barrier, a thin oxide layer was also added between the Schottky interface.

A. LSPR Induced Hot Carrier Effect

In recent years, research on surface plasmon-induced hot carrier effects has gained significant attention. Surface plasmon refers to the collective oscillation of electrons on a metal surface induced by external electromagnetic fields, and it exhibits unique optical and electronic properties distinct from bulk materials [29], [30], [31], [32]. When surface plasmons couple with incident photons, it leads to a highly efficient energy transfer [33], [34], [35], [36], [37], [38], enabling the absorption of longer-wavelength photons and conversion into hot carriers within the metal thin film layer [39], [40], [41], [42], [43], [44]. The aim of this work is to enhance the response of photodetectors in the infrared wavelength range by utilizing another surface plasmon effect, namely, localized surface plasmon resonance (LSPR) structures. In contrast to surface plasmon resonance (SPR), LSPR is generated through metal nanostructures, contributing to the enhancement of localized electric field distribution hotspots. The resonant wavelength of LSPR is closely related to the size and shape of the local structure, allowing for control by adjusting the characteristics of nanostructures [45], [46]. Although the effects of LSPR are similar to surface plasmon polaritons (SPP) generated by SPR, LSPR does not require the use of gratings, prisms, or subwavelength structures to match the incident wave vector for electromagnetic field coupling. Compared to SPR,

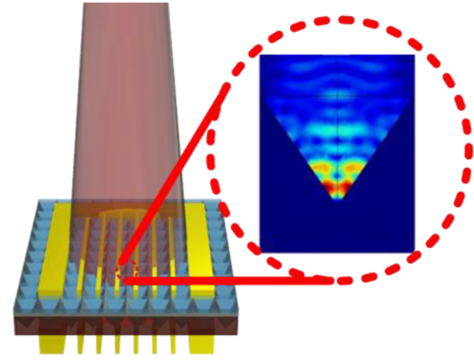

Fig. 1. Schottky photodetector with an inverted pyramid array structure.

LSPR has more relaxed coupling conditions and can easily achieve coupling with plasmon resonances and enhanced absorption of incident light by selecting different materials and adjusting the morphology of nanostructures [47], [48], [49]. To achieve the induction of localized surface plasmon resonance and optimize the light-responsive behavior in a super-wideband spectral range, this study explores a structure based on a novel concept, as depicted in Fig. 1, by combining a Schottky photodetector with an inverted pyramid structure (IPS). The height of the inverted pyramid cavities and the angle between each sidewall are set at 54.74°. Through near-field simulations with x- and y-polarized light incident on IPS, this structure is demonstrated to induce super-wideband localized surface plasmon resonance and exhibit excellent electric field distribution within the inverted pyramid cavities. Ultimately, through plasmon decay at the Schottky junction, a substantial number of hot carriers is generated, thereby enhancing the conversion efficiency.

COMSOL software allows us to simulate the LSPR intensity under different wavelength conditions. Simulating LSPR intensity for various surface structure sizes enables us to specifically compare the effect of size on the conversion of hot carriers. The simulation and modeling utilized a structure featuring an inverted pyramid array. Near-field simulations were carried out for x- and y-polarized light incidents on the inverted pyramid array to induce localized surface plasmon resonance (LSPR). The height of the inverted pyramid cavity and the angle between each sidewall were set at 54.74°, referencing the crystal orientation of the silicon substrate. Simulations conducted with COMSOL software explored LSPR intensities under different wavelength conditions, particularly focusing on simulating LSPR intensities for various structure sizes. The inverted pyramid structure used in these simulations is illustrated in Fig. 2(a), featuring a 10 nm Cr metal surface on the silicon substrate. Simulations involved x- and y-polarized light incident on the inverted pyramid structure (IPS), guiding light into the pyramid structure from the top. Fig. 2(b) provides the simulation results of the electric field for the LSPR structure on the IPS surface. The generation of hot carriers caused by plasma decay depends on photon absorption. Previous studies have demonstrated that the measured photocatalytic activity spectra or photocurrent response rates are related to the absorption spectra associated with the localized surface plasmon enhancement [51], [52]. Enhanced absorption

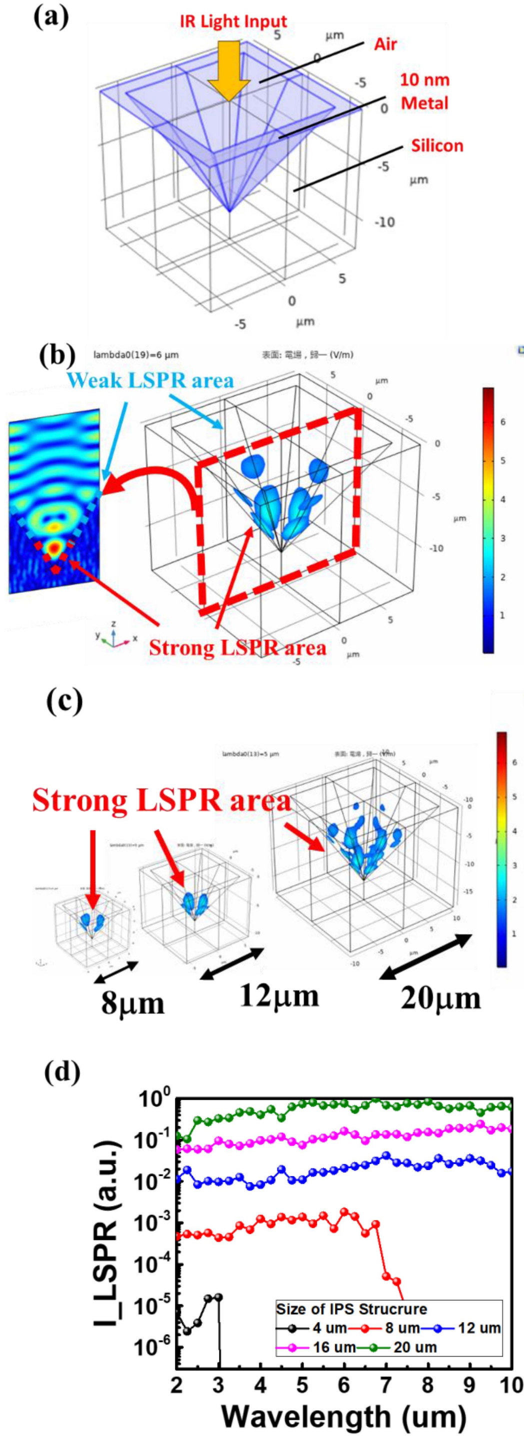

Fig. 2. (a) The inverted pyramid structure used in COMSOL simulations. (b) The result of the electric field simulation. (c) The simulation of COMSOL. (d) The total LSPR effects of pyramid structures with sizes of 4, 8, 12, 16, and 20 μm in the wavelength range of 2–10 μm.

spectra are further correlated with local field intensity (E) and area (A) [53], [54], [55]. It is noteworthy that the hot carriers with a distance from the photosensitive interface may undergo recombination, or other forms of energy loss. Only the hot carriers generated in regions meeting the conditions of localized surface plasmon enhancement and being closer to the interface than the mean free path can participate in the transfer of the hot electron energy. The area (A_{LSPR}) that meet the conditions of localized surface plasmon enhancement and mean free path is shown in Fig. 2(b). The impact of structural sizes on LSPR at the photoelectric conversion interface is illustrated in Fig. 2(c). Here, areas that do not meet the conditions of localized surface plasmon enhancement and mean free path are excluded to clearly present the distribution of areas (A_{LSPR}) meeting these conditions. The effects of the structural size on the localized surface plasmon resonance are related to the area parameter (A_{LSPR}). To quantify photon absorption, we use the parameter I_{LSPR} to define the enhanced light absorption intensity under different wavelengths, and compare the I_{LSPR} of components of different sizes, shown in Fig. 2(d).

$$I_{LSPR} = \int |E(A_{LSPR})|^2 \, dA \tag{1}$$

In Fig. 2(d), the I_{LSPR} parameter of pyramid structures with sizes ranging from 4 to 20 μm within the wavelength range of 2 to 10 μm are demonstrated. The I_{LSPR} curves are normalized with the I_{LSPR} curve of 20 μm pyramid structure and describe the results using arbitrary units, which provide a more intuitive representation of the enhanced photon absorption effect, as shown in Fig. 2(d). From the perspective of fixed wavelength bands, taking the 5 μm wavelength as an example, the relative intensity change of enhanced photon absorption produced by the pyramid structures of 4, 8, 12, 16, and 20 μm compared to the intensity of the 8 μm pyramid structure is 0, 1.00, 7.91, 54.2, and 529.1, respectively. In addition to observing that the pyramid structure provides a wide wavelength range of electric field resonance effects, we also found that the size of the structure is a crucial parameter that significantly limits the wavelength band of the LSPR. A pyramid structure with a size of 4 μm can only generate LSPR effects at wavelengths shorter than 4 μm, while a pyramid structure with a size of 8 μm can achieve LSPR effects at wavelengths shorter than 8 μm. Based on these findings, we subsequently fabricated pyramid structures with a size of 20 μm to achieve a broader LSPR range. Larger pyramid sizes correspond to higher I_{LSPR}, and larger structural sizes are also expected to correlate with stronger absorption spectra and higher optical responses.

B. Device Fabrication

This paper follows the fabrication method shown in Fig. 3(a) for a silicon-based LSPR structure proposed by our research team [26]. The process of LSPR structure includes the deposition of silicon dioxide (using PECVD), lithography process, dry etching, and wet etching to define the pattern on the silicon substrate. Notably, we encountered a fabrication challenge when scaling up the structure to a 20 μm full inverted pyramid array. The difference between the vertical and horizontal etching rates affects the uniformity of the LSPR structure in the KOH wet-etching process, which is particularly important during the long etching time required for the larger-period pyramid process technology.

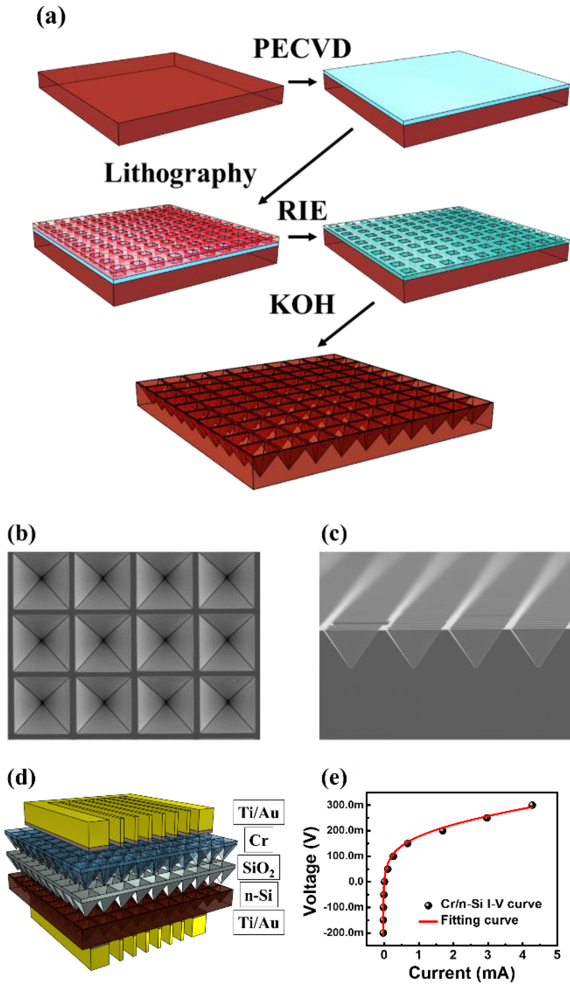

Fig. 3. LSPR structure: (a) process of silicon-based LSPR structure; (b) top view of LSPR structure using a scanning electron microscope; (c) side view of LSPR structure using a scanning electron microscope; (d) 3D schematic of LSPR Schottky device; (e) the current-voltage curve and the fitting parameters.

The uniformity of the LSPR structure is determined by the pattern of the silicon dioxide layer, which does not react with the KOH etching solution. When exposed to KOH, the silicon (Si) bonds on the substrate will combine with hydroxide ions (OH^-) to form $Si(OH)_2^{2+}$. Due to the high electronegativity of oxygen in $Si(OH)_2^{2+}$, the electrons in the Si–Si bond are continuously attracted to the hydroxide ions, which weakens the Si–Si bond. Because $Si(OH)_2^{2+}$ dissolves easily in water, the attracted Si–Si bond will eventually break. The different etching rates of the Si substrate (100) and (111) crystals result in the initial Si surface eventually being etched into an array of pyramidal structures whose size slowly increases with time. At the same time, the contact area between SiO_2 and Si keeps decreasing and hydrogen gas is continuously generated at the contact boundary. These 2 points may lead to the phenomenon of SiO_2 exfoliation. Once SiO_2 exfoliation occurs, irregular, random-sized pyramidal mounds appear on the Si substrate after the wet-etching process, instead of a periodic pyramidal distribution. To maintain the structural uniformity and avoid over-etching during the long etching time, the design of the mask is crucial. By adjusting the duty cycle of the pattern and precisely controlling the temperature of the etched KOH solution to reduce the different durations of vertical and horizontal etching, the flaking of the silica layer could be avoided and the structural homogeneity could be maintained under long etching times. The completeness of the pyramidal structure was confirmed through the scanning electron microscope images shown in Fig. 3(b) and (c). It is worth noting that previous works, such as reference [25], focused on the generation of randomly distributed pyramid structures to enhance such effects. While these studies observed enhanced responses and expanded detection spectrum, the lack of consistent and quantifiable features in randomly sized structures makes it challenging to effectively discuss the localized surface plasmon resonance effects from pyramids of different sizes across various spectral bands. In contrast, our structured approach here provides a systematic and quantitative exploration of ultra-broadband LSPR effects, laying the foundation for a more comprehensive understanding of the induced phenomena.

In metal/silicon interface photodetectors, the presence of Fermi level pinning [56], [57] limits the barrier height and further restricts the detectable wavelength range of nanoscale-metal/silicon interface infrared photodetectors. Since Fermi levels of two materials must align with each other at the interface, there exist gap states that decay deeper into the semiconductor, known as metal-induced gap states (MIGS) responsible for a pinning of the surface energy state regardless of the metal used, namely the Fermi-level pinning. Regardless of the metal used, there exists a barrier height of about 1/2 the semiconductor bandgap. The silicon substrate with inverted pyramid structure was placed in piranha solution to form a layer of SiO_2 with thickness much less than 10 nm on the surface of the pyramid structure. The insulating layer is to weaken the penetration of metal wave functions into the semiconductor, reducing MIGS and thus reducing the pinning effect [58], [59], [60]. Subsequently, 10-nm thick chromium film was evaporated by electron beam evaporator as the Schottky contact. On the other side of Si substrate, 10-nm thick titanium film was first evaporated as an attachment layer, and 100-nm thick gold was subsequently evaporated as a good conductive layer. So far, the surface plasma resonant Schottky infrared photodetector with inverted pyramid structure was completed. The component structure is shown in Fig. 3(d).

Furthermore, the determination of the theoretical barrier involves primarily utilizing the thermionic emission equation [61], [62], [63] to fit the I–V curves (Fig. 3(e)). In the thermionic emission equation, V and I represent the applied bias and experimentally measured current of the device, respectively. A, A∗, k, and q are known parameters representing the area of the device, Richardson constant, Boltzmann constant, and electron charge, respectively. Analysis parameters include Rs (series resistance), Φ_B (barrier height), T (temperature), and n (ideality factor). In our previous studies, the reliability of fitting results has been explored using multiple fitting verification methods. For Schottky devices, an equivalent circuit incorporating a series resistance can be employed to introduce an additional controllable series resistance as an experimental variable parameter. The measurement system for the device and

TABLE I
FITTING RESULTS OF IV CURVE WITH THE THERMIONIC EMISSION EQUATION [61], [62], [63]

Fitting Parameters	Value
Series resistance (Ω)	15.435
Ideality factor	1.8162
Barrier height (eV)	0.4775
Temperature (K)	290.08

external resistors involves a direct series connection, and the IV characteristic curves are recorded using a Keithley 2400 source meter. By evaluating the numerical error rates between fitting and actual added resistances, we can determine the most reliable parameter combinations among various fitting results. The theoretical barrier height was mainly determined by fitting the I–V curves (Fig. 3(e)) with the thermionic emission equation [61], [62], [63]. In Table I, the barrier height was found to be 0.4775 eV, which limits the long-wavelength detection threshold below 2600 nm.

III. DISCUSSION

A. Enhanced Mid-Infrared Response LSPR-Induced Hot Carrier Effect

The mid-infrared response measurement system is set up, as shown in Fig. 4(a). A heated ceramic chip emits broadband blackbody radiation from 2 μm to 24 μm, which is then filtered at 2700, 3460, 4260, and 5300 nm to output specific wavelengths that illuminate the Schottky device. The blackbody radiation's continuous output is converted to an optical signal of the on/off keying (OOK) type by an optical chopper. The filters used were bandpass filters manufactured by Edmund Optica, Inc. The Bruker vertex 70 Fourier transform infrared (FTIR) spectrometer was adopted to measure the transmittance spectra in the nitrogen atmosphere. The filter had a maximum of 70–80% peak penetration, with a bandwidth in the range of 200–600 nm. Besides, Vis-NIR spectroscopy was measured using a JASCO v770 spectrometer to confirm that no light leakage occurred in the visible and near-infrared regions.

Due to the weak signal of hot carriers, a low noise preamplifier (SR560) is used in the system to enhance the electrical signal before it enters the Oscilloscope (Tektronix TDS 3032B). During the measurement process, the gain of the low noise preamplifier (SR560) is set to 10^4 times. In order to obtain more accurate power values, a commercial III–V detector (Thorlabs PDA10PT) was used for signal measurements at different temperature light sources. Consequently, electrical signals converted by the Schottky device can be observed on an oscilloscope after amplification.

The device size is 2.5 × 2.5 cm^2, which is relatively large. Thus, the optical chopper used in the experiment cannot achieve rapid switching during the modulation of the light signal. This is why the measurement results in Fig. 3 exhibit a signal that closely resembles a sine wave. The signal frequency is set at

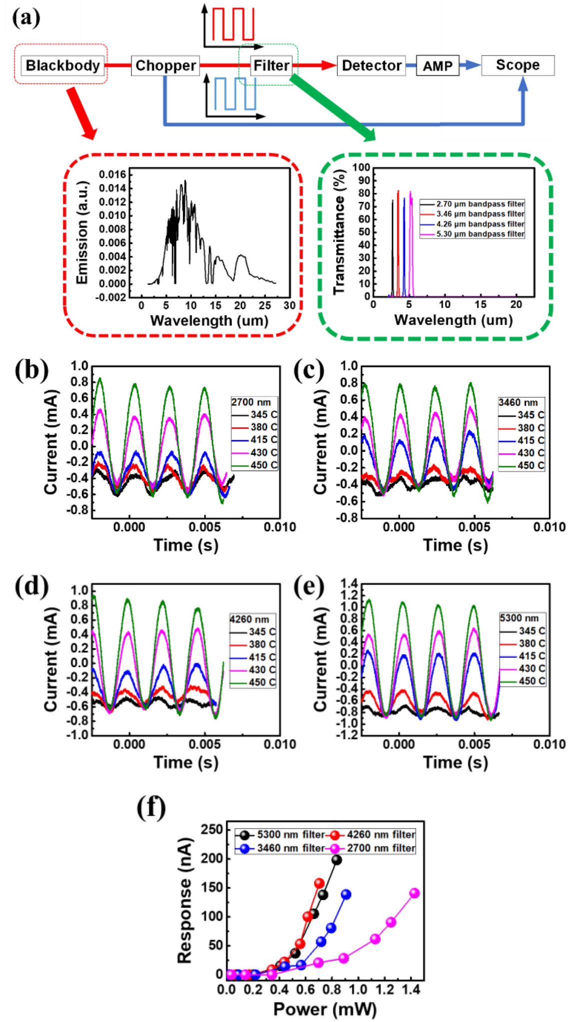

Fig. 4. Hot-carrier effect on silicon-based Schottky devices: (a) measurement setup, green field is the transmission spectrum of 2700, 3460, 4260, and 5300 nm band pass filters; (b)–(e) the measurement signal of the device at 2700, 3460, 4260, and 5300 nm band; (f) response plotted for different temperature light-source power on the device after filtering.

379 Hz, which is a prime number and significantly different from multiples of the 60 Hz of the AC equipment (light source) used in daily life, effectively improving the accuracy of the results. The blackbody radiation source's temperature is set from 25 °C to 450 °C. However, the signal is too small to measure until 345 °C. The current variation over time measured using the silicon-based Schottky device is also a signal in the OOK form. The highest and lowest data of the signal and the filtered source's power are taken into account.

Fig. 4(b)–(e) illustrate the infrared signal measurements of silicon-based Schottky devices at wavelengths of 2700, 3460, 4260, and 5300 nm. The trend of response variation with power can be obtained by calculating the variation in current levels. Fig. 4(f) shows that the response superlinearly increases with the incident light intensity. Another interesting phenomenon is that as the wavelength (μm) increases, the measured response gradually increases. The responsivities of hot carrier device for the 2700, 3460, 4260, and 5300 nm are 0.098, 0.152, 0.224,

and 0.237 mA/W, respectively. The explanation for these two phenomena lies in the hot carrier mechanism. When light irradiates a metal surface, it generates a surface plasmon. As the surface plasmon decays, its energy is transferred to the carrier, forming hot electrons. These generated hot electrons will diffuse towards the metal/silicon interface, gradually losing their energy during this process. To maximize the generation of hot carriers, the influence of surface plasmons is of paramount importance. Notably, the pyramid structure demonstrates a superior ability to generate a strong electric field resonance effect, compared to a planar structure, thereby enabling the experimental generation of a great number of hot carriers. This abundance of hot carriers enhances the potential for energy exchange among them. Moreover, this increased number of hot carriers lead to fast diffusion to the metal/silicon junction, increase the number of hot carriers with energy above the Schottky barrier, and so facilitate the detection under higher-intensity light conditions. This phenomenon is visually represented in Fig. 4(f), illustrating how the response exhibits a superlinear increase with the incident light intensity. Additionally, our simulations have provided another important insight. In addition to the broad wavelength range of the electric field resonance effect observed with the pyramidal structure, we have also identified a gradual increase in the electric field resonance strength as a function of wavelength in the optical field simulation of the 20 μm-sized pyramidal structure. The I_{LSPR} integrals have been found to increase from 6.6×10^{-31} to 2.1×10^{-30} ($V^2 \cdot m$) at incident wavelengths within the range of 2.7–5.3 μm, respectively. This observation aligns with our experimental results and indicates a consistent trend of increasing field strength with longer incident wavelengths. In summary, longer wavelengths of incident light in the 2–6 μm band generate stronger electric field strengths in the 20 μm structure, leading to more number of the hot carriers and thus higher measurement responsivity.

Detectivity is a significant indicator used to evaluate the superiority of detectors [64]. A higher detectivity value indicates a better-performing detector. Detectivity can be understood as the ratio of the signal-to-noise that a detector can generate for 1 W of incident light on an area of 1 cm^2 with a noise bandwidth of 1 Hz. By multiplying by the square root of the area, the detectivity also eliminates the area's effect, making it a more objective measure of the device's performance. The formula for detectivity is shown as (2):

$$D^* = \sqrt{A\Delta f}\,\frac{\mathrm{Responsivity}}{I_{\mathrm{Noise}}} \tag{2}$$

where A is the effective area of the detector (6.25 cm^2), R is the responsivity, Δf is the bandwidth, and I_{noise} represents the value of the 1 Hz noise spectral component. Table II lists the optimal responsivity and detectivity of the hot carrier devices in each wavelength band.

B. Response Speed of Hot Carrier Device

It is also interesting to investigate the response speed of such detectors using the hot-carrier effect. In the measurement system for different wavelengths illustrated in Fig. 4, we employed an optical chopper to modulate the light signal. This decision was made considering experiments involving a broadband infrared light source combined with infrared filters at different specific wavelengths. However, it is important to note that the optical chopper modulates the light signal through physical rotation, limiting the modulation frequency to the kHz level and preventing faster modulation. Thus, to explore the response speed of detectors with the hot carrier effect, in the section discussing frequency response, we chose a mid-infrared LED that can be electrically modulated to generate higher-frequency infrared signals.

TABLE II
THE OPTIMAL RESPONSIVITY AND DETECTIVITY OF THE HOT CARRIER DEVICES IN EACH WAVELENGTH

Wavelength (nm)	Responsivity (mA/W)	D*(cmHz$^{1/2}$W^{-1})
2700	0.098	3.230×10^8
3460	0.152	4.998×10^8
4260	0.224	7.336×10^8
5300	0.237	7.754×10^8

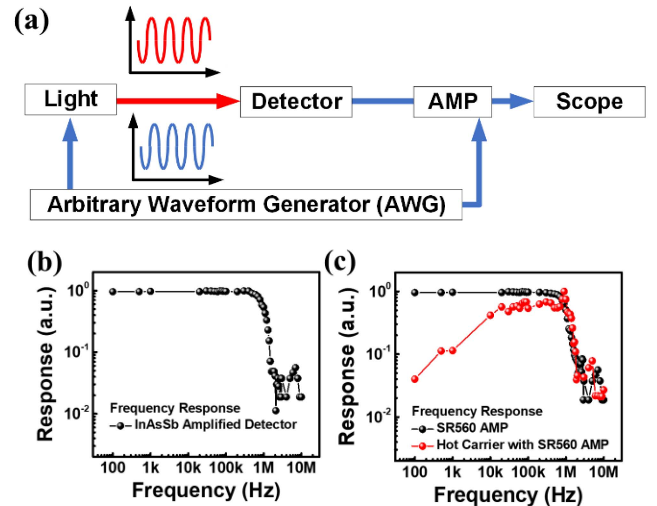

Fig. 5. (a) The measurement setup of infrared frequency response. (b) The frequency response of Thorlab InAsSb amplified photodetector. (c) The frequency response of the hot carrier device with pre-amplifier SR560 (red line) and the frequency response of the pre-amplifier SR560 (black line).

Fig. 5(a) shows the measurement system. A 4300 nm LED (Thorlab-4300W) served as the light source, modulated by a sinusoidal signal generated by a waveform generator with a frequency range from 0.1 kHz to 10 MHz. To prevent distortion of the LED output signal, the waveform generator not only provided a sinusoidal signal for the LED's periodic variation but also maintained an offset forward bias voltage to control the operational point of the signal modulation. Initially, we used a Thorlab InAsSb detector with an internal amplification circuit, with a limited 3 dB bandwidth to 1.6 MHz to verify the frequency response, as shown in the obtained data (Fig. 5(b)). This electrical modulation of the light signal allowed us to explore the frequency response by varying the modulation frequency.

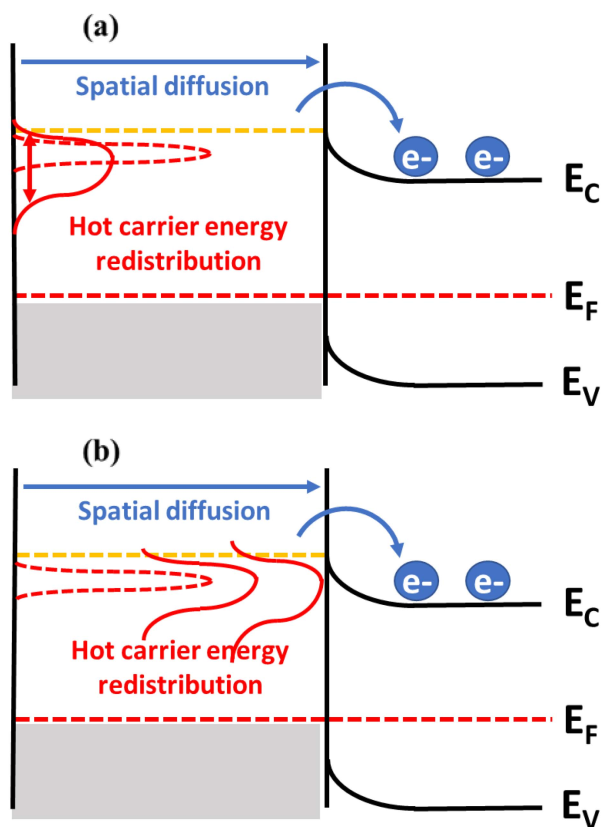

Fig. 6. Silicon-based hot carrier low-energy photon detection mechanism: (a) hot carrier energy redistribution; (b) hot carrier spatial diffusion.

Importantly, in these measurements, we maintained a constant pulse width and duty cycle, achieving modulation by changing the frequency of the sinusoidal signal. After checking with the commercial detector, we then measured the hot-carrier device and used a low-noise voltage preamplifier SR560 to amplify the signal. The frequency response of the hot-carrier device and pre-amplifier (SR560) is shown in Fig. 5(c). In the 3 dB frequency range of the pre-amplifier (SR560), the extremely thin metal material in the hot-carrier device facilitates the fast separation and transport of the photoexcited hot carriers, resulting in an increased response with frequency in the range from 0.1 to slightly above 1 MHz. The measured 3 dB bandwidth is 2.1 MHz, limited by the pre-amplifier (SR560) bandwidth. Hence, the response speed of the hot-carrier device is faster than 1 μs. In comparison, the response speed of a typical silicon-based bolometer is around 5 ms [65]. With assistance from nanometallic antennas, the response speed of silicon-based bolometers can be accelerated to 3∼13 μs [19], [20]. The ultra-fast response speed of the hot-carrier Schottky chip makes its potential applications superior to those of bolometers.

Importantly, the phenomenon causing the device to sense photons with wavelengths >2700 nm is attributed to multiple excitations, specifically the mechanism of hot carriers. According to the energy conversion principle in the theory of hot carriers, carriers in the metal layer, upon absorbing energy, generate hot carriers. These hot carriers can surpass the work function effect and transition to another material state through energy conversion [66], [67]. When the incident light injects hot carrier generation, it initiates a series of collisions between hot carriers and the lattice, as well as energy exchange between cold carriers and hot carriers [68], [69], [70]. Such a process greatly expands the measurable spectral range, surpassing the measurement limit typically caused by energy gaps [71], [72], [73], as illustrated in the diagram below. Furthermore, we do not deny that some of the measured responses may be attributed to tunneling effects, as theoretically, the occurrence of tunneling effects is not zero. Therefore, both discussing the combined effects of tunneling and hot carrier mechanisms, as well as distinguishing between tunneling and hot carrier effects, will be one of the directions for future research.

The reason for the ultra-fast response speed of the hot-carrier device can also be explained by hot carrier theory. In Fig. 7, electrons of different colors represent carriers with different energy levels. Fig. 7(a) illustrates the process of hot carrier excitation, where gray electrons in the ground state are excited to become red hot carriers through the absorption of light. In Fig. 7(b), the process of spatial and energy diffusion is shown. During this stage, the energy of the hot carriers gradually changes from red to yellow and blue. Yellow hot carriers represent higher energy levels compared to the red hot carriers excited by light, while blue indicates lower energy levels than the red hot carriers excited by light. At the Schottky interface, the hot carriers (yellow) with energy higher than the barrier can overcome the barrier height, generating a photocurrent. On the other hand, the hot carriers with insufficient energy (blue) cannot pass the barrier. These carriers accumulate at the interface and affect the subsequent energy distribution of the hot carriers during continuous irradiation. In Fig. 7(c) and (d), the diffusion process of carriers is shown when low-energy hot carriers accumulate at the interface. Due to the presence of low-energy hot carriers at the interface, subsequently, excited hot carriers (brown) do not possess higher energy than the initially excited thermal carriers (yellow) because the low-energy hot carriers will interact with the high-energy hot carriers, effectively reducing the number of high-energy hot carriers.

Additionally, accumulated charges at the interface generate an electric field in space. This electric field may impact the diffusion of hot carriers, and the specific degree of influence depends on the strength and direction of the electric field. Since the electric field's direction is opposite to the diffusion direction of hot carriers, it applies resistance, affecting the motion of hot carriers. The electric field imparts field forces on carriers, hindering their migration. Initially, under illumination, the energy barrier at the interface blocks some hot carriers. Although over time the number of hot carriers unable to overcome the energy barrier decreases, those unable to rapidly descend to the Fermi level at the next time point will impact incoming hot carriers. After energy exchange, subsequent hot carriers exhibit less energy, making it more challenging for them to overcome the energy barrier and generate electrical signals. These low-energy hot carriers accumulate over time, increasingly affecting high-energy hot carriers, resulting in fewer and fewer hot carriers overcoming the energy barrier. As time progresses, due to the offsetting of the decayed carriers with the generated carriers, the number of

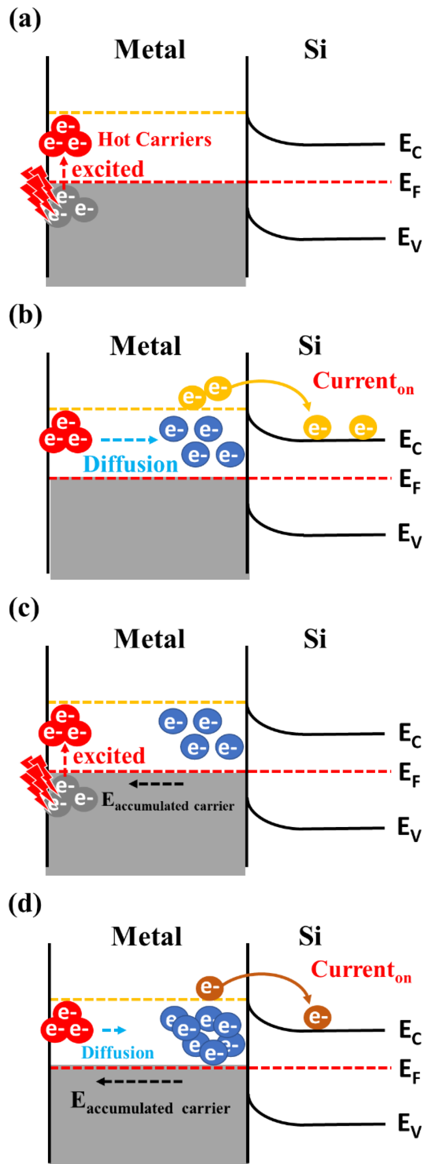

Fig. 7. The four-step hot carrier dynamic theory of hot electron in metal material. (a) The process of hot carrier excitation. (b) The process of spatial and energy diffusion. (c) The process of hot carrier excitation when low-energy hot carriers accumulate at the interface. (d) The process of spatial and energy diffusion when low-energy hot carriers accumulate at the interface.

carriers accumulating at the interface does not increase in quantity but maintains a dynamic equilibrium between generation and decay. When charges are present near the interface, they create an electric field that exerts forces on electrons and hot carriers moving in that region, potentially hindering or promoting the diffusion of hot carriers. This process causes a stable frequency response in the 100 kHz to 1 MHz range but a rapid decline in the frequency range below 10 kHz.

V. Conclusion

In the research of Schottky devices, the internal photoemission (IPE) mechanism and the Schottky barrier height have been considered as the main factors for detecting optical signals. Light with energy lower than the barrier height is considered unable to be detected. However, this work explores the utilization of the hot carrier effect in nanoscale metal materials to effectively collect hot carriers before decay, and extends mid-infrared detection to wavelengths of about 5.3 μm. Besides, the periodically arranged inverted pyramid structure was developed to achieve a broad-spectrum LSPR, including the mid-infrared range. With a strong LSPR structure, the responsivities were increased from the nA/W to near mA/W scale. Even at wavelengths up to 5.3 μm, the hot carrier mechanism also led to the responsivity of hot carrier device up to 0.237 mA/W. As a result, this work reveals a broadband optoelectronic detector capable of detecting wavelengths from 2.7 to 5.3 μm. Moreover, the 3 dB bandwidth of the hot carrier device is found to be 2.1 MHz in this study. In the future, this high-speed and low-energy photon sensing silicon-based technology may be combined with current silicon-based complementary metal-oxide-semiconductor (CMOS) technology to further achieve lower cost silicon-based mid-infrared semiconductor integrated chips.

Acknowledgment

The authors thank Y.T. Lee of the Instrumentation Center, National Taiwan University, for FEG-SEM experiments.

Disclosures

The authors declare no competing financial interests or conflicts of interest.

Data Availability

The datasets used and/or analyzed during the current study available from the corresponding author on reasonable request.

References

[1] S. Cha et al., "1s-intraexcitonic dynamics in monolayer MoS_2 probed by ultrafast mid-infrared spectroscopy," *Nature Commun.*, vol. 7, 2016, Art. no. 10768.
[2] M. D. Karín et al., "Mid-infrared spectroscopy of submillimeter galaxies: Extended star formation in massive high-redshift galaxies," *Astrophysical J.*, vol. 699, 2009, Art. no. 667.
[3] N. Robert et al., "Remote near infrared identification of pathogens with multiplexed nanosensors," *Nature Commun.*, vol. 11, 2020, Art. no. 5995.
[4] L. Zeng, B. Li, R. Wen, and X. Zhang, "Plasmonic sensor based on multi fano resonance in inverse T shape structure for detection of CO_2 concentration," *IEEE Photon. J.*, vol. 15, no. 5, Oct. 2023, Art. no. 2201805.
[5] J. Shi et al., "High-resolution, high-contrast mid-infrared imaging of fresh biological samples with ultraviolet-localized photoacoustic microscopy," *Nature Photon.*, vol. 13, pp. 609–615, 2019.
[6] L. C. Hirst et al., "Enhanced hot-carrier effects in InAlAs/InGaAs quantum wells," *IEEE J. Photovolt.*, vol. 4, no. 6, pp. 1526–1531, Nov. 2014.
[7] D. Fan et al., "Near-perfect photon utilization in an air-bridge thermophotovoltaic cell," *Nature*, vol. 586, pp. 237–241, 2020.
[8] H. Esmaielpour et al., "Exploiting intervalley scattering to harness hot carriers in III–V solar cells," *Nature Energy*, vol. 5, pp. 336–343, 2020.
[9] Y. Xue et al., "High-performance III-V photodetectors on a monolithic InP/SOI platform," *Optica*, vol. 8, pp. 1204–1209, 2021.
[10] J. Miao et al., "Single InAs nanowire room-temperature near-infrared photodetectors," *ACS Nano*, vol. 8, pp. 3628–3635, 2014.
[11] C. H. Kuo et al., "High sensitivity of middle-wavelength infrared photodetectors based on an individual InSb nanowire," *Nanoscale Res. Lett.*, vol. 8, pp. 1–8, 2013.
[12] H. Kumar and C.-H. Lin, "High-performance lateral metal-germanium-metal SWIR photodetectors using a-Si: H interlayer for dark current reduction," *IEEE Photon. J.*, vol. 15, no. 1, Feb. 2023, Art. no. 6800408.

[13] A. Chu et al., "Infrared photoconduction at the diffusion length limit in HgTe nanocrystal arrays," *Nature Commun.*, vol. 12, 2021, Art. no. 1794.
[14] C. Cheng et al., "Monolithic optoelectronic integrated broadband optical receiver with graphene photodetectors," *Nanophotonics*, vol. 6, pp. 1343–1352, 2017.
[15] X. Yu, Z. Dong, J. K. Yang, and Q. J. Wang, "Room-temperature mid-infrared photodetector in all-carbon graphene nanoribbon-C 60 hybrid nanostructure," *Optica*, vol. 3, pp. 979–984, 2016.
[16] A. I. Yakimov et al., "Photovoltaic Ge/SiGe quantum dot mid-infrared photodetector enhanced by surface plasmons," *Opt. Exp.*, vol. 25, pp. 25602–25611, 2017.
[17] J. Huang, S. Yan, T. Xue, Y. Zhang, and W. Ma, "Mid-wavelength InAs/InAsSb superlattice photodetector with background limited performance temperature higher than 160 K," *IEEE Trans. Electron Devices*, vol. 69, no. 8, pp. 4392–4395, Aug. 2022.
[18] X. Dai et al., "GaAs/AlGaAs nanowire photodetector," *Nano Lett.*, vol. 14, pp. 2688–2693, 2014.
[19] D. Elamaran, Y. Suzuki, H. Satoh, A. Banerjee, N. Hiromoto, and H. Inokawa, "Performance comparison of SOI-based temperature sensors for room-temperature terahertz antenna-coupled bolometers: MOSFET, PN junction diode and resistor," *Micromachines*, vol. 11, 2020, Art. no. 718.
[20] Y. Wu et al., "Mid-infrared nanometallic antenna assisted silicon waveguide based bolometers," *ACS Photon.*, vol. 6, pp. 3253–3260, 2019.
[21] A. D. Pris et al., "Towards high-speed imaging of infrared photons with bio-inspired nanoarchitectures," *Nature Photon.*, vol. 6, no. 3, pp. 195–200, 2012.
[22] M. W. Knight, H. Sobhani, P. Nordlander, and N. J. Halas, "Photodetection with active optical antennas," *Science*, vol. 332, pp. 702–704, 2011.
[23] W. Li and J. G. Valentine, "Harvesting the loss: Surface plasmon-based hot electron photodetection," *Nanophotonics*, vol. 6, pp. 177–191, 2017.
[24] Z. Qi et al., "Au nanoparticle-decorated silicon pyramids for plasmon-enhanced hot electron near-infrared photodetection," *Nanotechnology*, vol. 28, 2017, Art. no. 275202.
[25] Y. Zhai et al., "Hot electron generation in silicon micropyramids covered with nanometer-thick gold films for near-infrared photodetectors," *ACS Appl. Nano Mater.*, vol. 3, pp. 149–155, 2020.
[26] H. J. Syu et al., "Ultra-broadband photoresponse of LSPR from Si-based pyramid structures," *Photon. Res.*, vol. 7, pp. 1119–1126, 2019.
[27] Z.-C. Su and C.-F. Lin, "Overcoming the Fermi-level pinning effect in the nanoscale metal and silicon interface," *Nanomaterials*, vol. 13, no. 15, 2023, Art. no. 2193.
[28] Y.-C. Huang, V. Parimi, W.-C. Chang, H.-J. Syu, Z.-C. Su, and C.-F. Lin, "Silicon-based photodetector for infrared telecommunication applications," *IEEE Photon. J.*, vol. 13, no. 2, Apr. 2021, Art. no. 6800707.
[29] A. Y. Bykov et al., "Dynamics of hot carriers in plasmonic heterostructures," *Nanophotonics*, vol. 10, pp. 2929–2938, 2021.
[30] C. L. Petersen and S. A. Lyon, "Observation of hot-electron energy loss through the emission of phonon-plasmon coupled modes in GaAs," *Phys. Rev. Lett.*, vol. 65, 1990, Art. no. 760.
[31] D. Sicault, R. Teissier, F. Pardo, J. L. Pelouard, and F. Mollot, "Experimental study of hot-electron inelastic scattering rate in p-type InGaAs," *Phys. Rev. B*, vol. 65, 2002, Art. no. 121301.
[32] J. Lehmann, M. Merschdorf, W. Pfeiffer, A. Thon, S. Voll, and G. Gerber, "Surface plasmon dynamics in silver nanoparticles studied by femtosecond time-resolved photoemission," *Phys. Rev. Lett.*, vol. 85, 2000, Art. no. 2921.
[33] Y. F. Lao, A. G. Perera, L. H. Li, S. P. Khanna, E. H. Linfield, and H. C. Liu, "Tunable hot-carrier photodetection beyond the bandgap spectral limit," *Nature Photon.*, vol. 8, pp. 412–418, 2014.
[34] T. P. White and K. R. Catchpole, "Plasmon-enhanced internal photoemission for photovoltaics: Theoretical efficiency limits," *Appl. Phys. Lett.*, vol. 101, 2012, Art. no. 073905.
[35] B. Desiatov, I. Goykhman, N. Mazurski, J. Shappir, J. B. Khurgin, and U. Levy, "Plasmonic enhanced silicon pyramids for internal photoemission Schottky detectors in the near-infrared regime," *Optica*, vol. 2, pp. 335–338, 2015.
[36] Z. C. Su, Y. H. Li, and C. F. Lin, "Mid-infrared response from Cr/n-Si schottky junction with an ultra-thin Cr metal," *Nanomaterials*, vol. 12, 2022, Art. no. 1750.
[37] A. Nicarel et al., "Fourier two-temperature model to describe ultrafast laser pulses interaction with metals: A novel mathematical technique," *Phys. Lett. A*, vol. 392, 2021, Art. no. 127155.
[38] A. Block et al., "Tracking ultrafast hot-electron diffusion in space and time by ultrafast thermomodulation microscopy," *Sci. Adv.*, vol. 5, 2019, Art. no. eaav8965.
[39] M. Y. Semenov, "Control of heat-resistant steel carburized layer structure," *Part II. Metal Sci. Heat Treat.*, vol. 55, pp. 316–321, 2013.
[40] A. Einstein, "Über einem die Erzeugung und Verwandlung des Lichtes betreffenden Heuristischen Gesichtspunkt," *Annalen der Physic*, vol. 6, pp. 132–148, 1905.
[41] T. P. White and K. R. Catchpole, "Plasmon-enhanced internal photoemission for photovoltaics: Theoretical efficiency limits," *Appl. Phys. Lett.*, vol. 101, 2012, Art. no. 073905.
[42] P. Howard *Partial Differential Equations in Matlab 7.0*. College Park, MD, USA: Univ. of Maryland, 2005.
[43] J. Ma, Z. Wang, and L. W. Wang, "Interplay between plasmon and single-particle excitations in a metal nanocluster," *Nature Commun.*, vol. 6, 2015, Art. no. 10107.
[44] M. Bauer, A. Marienfeld, and M. Aeschlimann, "Hot electron lifetimes in metals probed by time-resolved two-photon photoemission," *Prog. Surf. Sci.*, vol. 90, pp. 319–376, 2015.
[45] C. F. Bohren and D. R. Huffman, *Absorption and Scattering of Light by Small Particles*. Hoboken, NJ, USA: Wiley, 2008.
[46] J. Jatschka et al., "Propagating and LSPR sensing—A critical comparison based on measurements and theory," *Sens. Bio-Sens. Res.*, vol. 7, pp. 62–70, 2016.
[47] K. S. Phillips, *Surface Plasmon Resonance-Based Sensors*, J. Homola, Ed. Berlin, Germany: Springer, 2008, pp. 1221–1222.
[48] P. Du et al., "Synthesis of thermally stable Ag@TiO2 core–shell nanoprisms and plasmon–enhanced optical properties for a P3HT thin film," *RSC Adv.*, vol. 3, no. 17, pp. 6016–6021, 2013.
[49] R. Lu et al., "A localized surface plasmon resonance and light confinement-enhanced near-infrared light photodetector," *Laser Photon. Rev.*, vol. 10, no. 4, pp. 595–602, 2016.
[50] V. E. Vickers, "Model of Schottky barrier hot-electron-mode photodetection," *Appl. Opt.*, vol. 10, no. 9, pp. 2190–2192, 1971.
[51] R. H. Fowler, "The analysis of photoelectric sensitivity curves for clean metals at various temperatures," *Phys. Rev.*, vol. 38, no. 1, pp. 45–56, 1931.
[52] M. Casalino, "Internal photoemission theory: Comments and theoretical limitations on the performance of near-infrared silicon Schottky photodetectors," *IEEE J. Quantum Electron.*, vol. 52, no. 4, Apr. 2016, Art. no. 4000110.
[53] S. Linic, P. Christopher, and D. B. Ingram, "Plasmonic-metal nanostructures for efficient conversion of solar to chemical energy," *Nature Mater.*, vol. 10, pp. 911–921, 2011.
[54] C. Clavero, "Plasmon-induced hot-electron generation at nanoparticle/metal-oxide interfaces for photovoltaic and photocatalytic devices," *Nature Photon.*, vol. 8, pp. 95–103, 2014.
[55] B. Y. Zheng et al., "Distinguishing between plasmon-induced and photoexcited carriers in a device geometry," *Nature Commun.*, vol. 6, no. 1, 2015, Art. no. 7797.
[56] C. Kim et al., "Fermi level pinning at electrical metal contacts of monolayer molybdenum dichalcogenides," *ACS Nano*, vol. 11, pp. 1588–1596, 2017.
[57] H. Yuan et al., "Influence of metal–MoS_2 interface on MoS_2 transistor performance: Comparison of Ag and Ti contacts," *ACS Appl. Mater. Interfaces*, vol. 7, pp. 1180–1187, 2015.
[58] D. Connelly, C. Faulkner, A. Clifton, and D. E. Grup, "Fermi-level depinning for low-barrier Schottky source/drain transistors," *Appl. Phys. Lett.*, vol. 88, 2006, Art. no. 012105.
[59] R. Islam, G. Shine, and K. C. Saraswat, "Schottky barrier height reduction for holes by Fermi level depinning using metal/nickel oxide/silicon contacts," *Appl. Phys. Lett.*, vol. 105, 2014, Art. no. 182103.
[60] Z.-C. Su and C.-F. Lin, "Overcoming the fermi-level pinning effect in the nanoscale metal and silicon interface," *Nanomaterials*, vol. 13, no. 15, 2023, Art. no. 2193.
[61] T. Zhang et al., "Measure and analysis of 4H-SiC Schottky barrier height with Mo contacts," *Eur. Phys. J. Appl. Phys.*, vol. 85, no. 1, 2019, Art. no. 10102, doi: 10.1051/epjap/2019190266.
[62] İ. Orak et al., "The analysis of the electrical and photovoltaic properties of Cr/p-Si structures using current-voltage measurements," *Silicon*, vol. 10, no. 5, pp. 2109–2116, 2018, doi: 10.1007/s12633-017-9681-1.
[63] C. Raynaud et al., "Barrier height determination of SiC Schottky diodes by capacitance and current–voltage measurements," *J. Appl. Phys.*, vol. 91, no. 12, pp. 9841–9847, 2002, doi: 10.1063/1.1478697.
[64] C. H. Ji, K. T. Kim, and S. Y. Oh, "High-detectivity perovskite-based photodetector using a Zr-doped TiOx cathode interlayer," *RSC Adv.*, vol. 8, no. 15, pp. 8302–8309, 2018, doi: 10.1039/C7RA13462A.
[65] Y. Wu et al., "Nanometallic antenna-assisted amorphous silicon waveguide integrated bolometer for mid-infrared," *Opt. Lett.*, vol. 46, pp. 677–680, 2021.

[66] X. Yu, Z. Dong, J. K. Yang, and Q. J. Wang, “Room-temperature mid-infrared photodetector in all-carbon graphene nanoribbon-C 60 hybrid nanostructure,” *Optica*, vol. 3, pp. 979–984, 2016.

[67] A. I. Yakimov et al., “Photovoltaic Ge/SiGe quantum dot mid-infrared photodetector enhanced by surface plasmons,” *Opt. Exp.*, vol. 25, pp. 25602–25611, 2017.

[68] J. Huang, S. Yan, T. Xue, Y. Zhang, and W. Ma, “Mid-wavelength InAs/InAsSb superlattice photodetector with background limited performance temperature higher than 160 K,” *IEEE Trans. Electron Devices*, vol. 69, no. 8, pp. 4392–4395, Aug. 2022.

[69] X. Dai et al., “GaAs/AlGaAs nanowire photodetector,” *Nano Lett.*, vol. 14, pp. 2688–2693, 2014.

[70] D. Elamaran, Y. Suzuki, H. Satoh, A. Banerjee, N. Hiromoto, and H. Inokawa, “Performance comparison of SOI-based temperature sensors for room-temperature terahertz antenna-coupled bolometers: MOSFET, PN junction diode and resistor,” *Micromachines*, vol. 11, 2020, Art. no. 718.

[71] Y. Wu et al., “Mid-infrared nanometallic antenna assisted silicon waveguide based bolometers,” *ACS Photon.*, vol. 6, pp. 3253–3260, 2019.

[72] A. D. Pris et al., “Towards high-speed imaging of infrared photons with bio-inspired nanoarchitectures,” *Nature Photon.*, vol. 6, no. 3, pp. 195–200, 2012.

[73] M. W. Knight, H. Sobhani, P. Nordlander, and N. J. Halas, “Photodetection with active optical antennas,” *Science*, vol. 332, pp. 702–704, 2011.